nature nanotechnology

ARTICLES

PUBLISHED ONLINE: XX XX 2016 | DOI: 10.1038/NNANO.2016.25

Nanopatterning reconfigurable magnetic landscapes via thermally assisted scanning probe lithography

E. Albisetti[1,2]*, D. Petti[1], M. Pancaldi[3], M. Madami[4], S. Tacchi[5], J. Curtis[2], W. P. King[6], A. Papp[7], G. Csaba[7], W. Porod[7], P. Vavassori[3,8], E. Riedo[2,9]* and R. Bertacco[1,10]*

The search for novel tools to control magnetism at the nanoscale is crucial for the development of new paradigms in optics, electronics and spintronics. So far, the fabrication of magnetic nanostructures has been achieved mainly through irreversible structural or chemical modifications. Here, we propose a new concept for creating reconfigurable magnetic nanopatterns by crafting, at the nanoscale, the magnetic anisotropy landscape of a ferromagnetic layer exchange-coupled to an antiferromagnetic layer. By performing localized field cooling with the hot tip of a scanning probe microscope, magnetic structures, with arbitrarily oriented magnetization and tunable unidirectional anisotropy, are reversibly patterned without modifying the film chemistry and topography. This opens unforeseen possibilities for the development of novel metamaterials with finely tuned magnetic properties, such as reconfigurable magneto-plasmonic and magnonic crystals. In this context, we experimentally demonstrate spatially controlled spin wave excitation and propagation in magnetic structures patterned with the proposed method.

Metamaterials are composite materials in which new functionalities emerge from engineered combinations of carefully chosen and nanoscale designed material building blocks[1–4]. Among these, magnetic metamaterials allow unprecedented versatility in the design of novel device architectures, exploiting the controlled propagation of electromagnetic radiation[1], surface plasmons[5,6] and spin waves[7–9]. In this context, the development of a new class of reprogrammable magnetic metamaterials, the functionality of which can be actively redesigned on demand, would open new, far-reaching directions for nanomagnetism and spintronics.

To date, the fabrication of magnetic devices through the nanopatterning of magnetic materials[10–12] has been carried out mainly using conventional lithography[10,13] or ion irradiation[11,12]. These techniques, in most cases, are irreversible, and their ability to finely control the modulation of the magnetic properties within the pattern is limited. Beyond these methods, advanced scanning-probe-based lithography (SPL) is gaining attention in the scientific community for its flexibility and broad applicability with emerging new materials[14].

In this Article, we propose a novel, versatile approach based on SPL—'thermally assisted magnetic scanning probe lithography' (*tam*-SPL)—to achieve a desired and reconfigurable nanoscale engineering of the magnetic properties of a continuous film. The working principle of *tam*-SPL is the local heating and cooling of an exchange-biased ferromagnetic layer by bringing the hot tip of a scanning probe microscope (SPM) into contact with a sample, in the presence of a magnetic field. This local field cooling sets a unidirectional magnetic anisotropy in the ferromagnetic due to exchange-coupling with the adjacent antiferromagnet[15]. Phenomenologically, this causes a local pinning of the ferromagnetic magnetization, which is observed as a shift in its hysteresis loop. Here, we demonstrate, in particular, the patterning of micro- and nanostructures with arbitrary shape, anisotropy and spin orientation. The pattern is stable at room temperature and cannot be erased permanently with magnetic fields, thus combining endurance and reconfigurability. These features can be exploited in the emerging field of magnonics to fabricate structures for the active manipulation of spin waves. As a proof-of-concept experiment, we show that local control of the spin wave excitation and propagation can be obtained in reconfigurable magnetic tracks patterned with *tam*-SPL.

Working principle of *tam*-SPL

Magnetic patterning was performed on a Ru(2)/IrMn(7)/CoFeB(5)/SiO_2(1,000)/Si (thicknesses in nm) multilayer structure, grown by magnetron sputtering, in which the IrMn/CoFeB bilayer constitutes the exchange bias system. For details of the growth and magnetic characterization of the non-patterned stack, see Methods and the Supplementary Information.

The working principle of *tam*-SPL is illustrated schematically in Fig. 1. The exchange bias system is first initialized by heating the entire sample above the blocking temperature T_B and subsequently cooling it in a uniform magnetic field H_i. This initialization sets a uniform unidirectional (UD) anisotropy axis in the ferromagnet film (Fig. 1a), with its hysteresis loop shifted by the exchange bias field H_e (Fig. 1d; see Methods for details). The hot tip of the SPM[16–20] is then used to locally heat the surface of the stack above T_B (160 °C) in a uniform static magnetic field $H_w = 700$ Oe, which in this particular case is chosen to be opposite the initialization

[1]Dipartimento di Fisica, Politecnico di Milano, 20133 Milano, Italy. [2]School of Physics, Georgia Institute of Technology, Atlanta, Georgia 30332, USA. [3]CIC nanoGUNE, E-20018 Donostia-San Sebastian, Spain. [4]Dipartimento di Fisica e Geologia, Università di Perugia, 06123 Perugia, Italy. [5]Istituto Officina dei Materiali del CNR (CNR-IOM), Unità di Perugia, c/o Dipartimento di Fisica e Geologia, 06123 Perugia, Italy. [6]Department of Mechanical Science and Engineering, University of Illinois Urbana-Champaign, Urbana, Illinois 61801, USA. [7]Center for Nano Science and Technology, University of Notre Dame, Notre Dame, Indiana 46556, USA. [8]IKERBASQUE, Basque Foundation for Science, 48011, Bilbao, Spain. [9]CUNY-Advanced Science Research Center and City College New York, City University of New York, 85 St Nicholas Terrace, New York, New York 10031, USA. [10]IFN-CNR, c/o Politecnico di Milano, Piazza Leonardo da Vinci, 32, 20133 Milano, Italy. *e-mail: edoardo.albisetti@polimi.it; elisa.riedo@asrc.cuny.edu; riccardo.bertacco@polimi.it

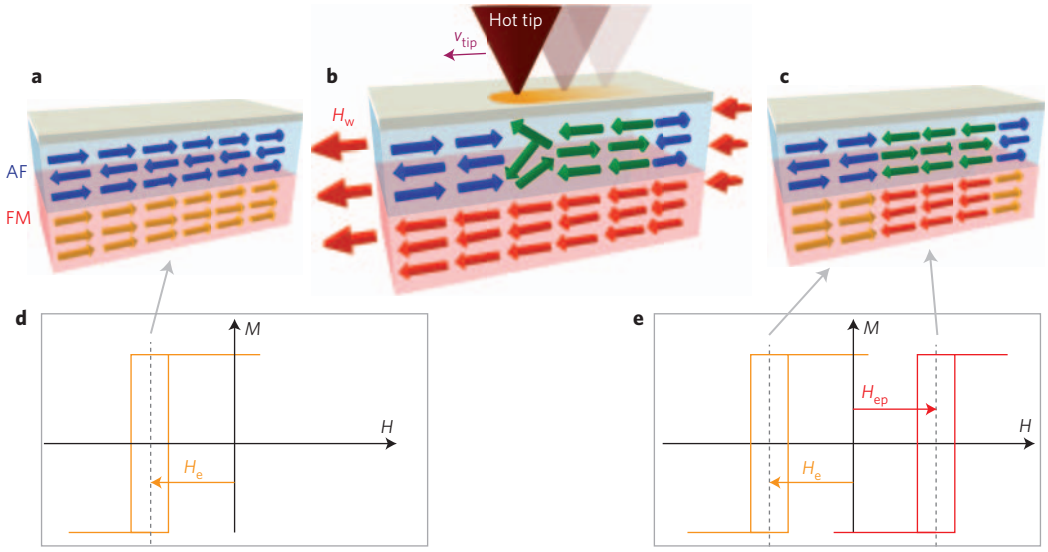

Figure 1 | Magnetic patterning via *tam*-SPL. a, After initialization, magnetization of the ferromagnetic (FM) layer (yellow arrows) is uniformly pinned in one direction by the exchange interaction with the antiferromagnetic (AF) layer (blue arrows). **b**, Sweeping a heated SPM tip on the sample surface in the presence of an external magnetic field H_w produces a local field cooling in the antiferromagnet (green arrows), which resets the exchange bias direction according to the underlying CoFeB spins (red arrows), aligned with H_w. **c**, When the external magnetic field H_w is removed, the magnetic domain configuration in the ferromagnet is stabilized by the local exchange bias. **d**,**e**, Magnetic hysteresis loops before (**d**) and after (**e**) patterning. H_e and H_{ep} indicate the opposite shift in the loops due to the exchange bias in the non-patterned and patterned areas, respectively.

field H_i. When the hot tip is displaced in its motion along the writing direction, the previously heated region of the antiferromagnet film undergoes a 'local field cooling' accompanied by a local rearrangement of the spins, due to coupling with the underlying ferromagnet oriented in the direction of the external field, H_w (Fig. 1b). Therefore, at the antiferromagnet–ferromagnet interface in the patterned area, a different local exchange bias is established, which shifts the local hysteresis loop to the right by a new exchange bias field H_{ep} (Fig. 1e). On removal of the writing field H_w, the local remanent magnetization within the ferromagnet layer is determined by the new UD magnetic anisotropy. As a result, the spins of the ferromagnet in the patterned area (red arrows in Fig. 1c) are antiparallel to those of the surrounding film (yellow arrows), which has switched back to the initial state.

Patterning capabilities

The patterning capabilities of this technique are demonstrated in Fig. 2. Square pads (sides of 20 μm) were first defined by optical lithography to facilitate navigation on the sample. *tam*-SPL was then used to define in the pad square, triangular and diamond-shaped structures with different lateral sizes (from 1.5 to 2.5 μm, Fig. 2a), with a writing speed of 3 μm s^{-1}. The SPM heater temperature T_H was set to 560, 675 and 765 °C for squares, triangles and diamonds, respectively. These T_H values ensure that the actual temperature at the tip–sample interface is well above T_B (Supplementary Fig. 2). H_w was set antiparallel to H_i to write structures with antiparallel remanent magnetization. For more details on the patterning conditions, see Methods and the Supplementary Information, where a general model for heat flow analysis developed for thermochemical (*tc*-)SPL[18] has been adapted to the present case. Figure 2a presents a magnetic force microscopy (MFM) image of a pad, taken at zero external field (remanent state) after *tam*-SPL, and Fig. 2b shows the topography of the same area. The opposite MFM magnetic contrast seen at the left and right edges of the patterns with respect to that at the pad edges demonstrates that regions with opposite UD anisotropy and remanent magnetization have been written by *tam*-SPL. We note that *tam*-SPL does not alter the morphology of the films (Fig. 2b) and that the patterning is therefore 'purely magnetic'. A zoomed-in MFM image of the pad area is shown in Fig. 2c. Although the diamonds were written at a much higher temperature than the squares, the resulting magnetic contrast is the same for all patterned structures, thus indicating that once the blocking temperature of the system is exceeded, reproducible patterns can be obtained without the need for precise control of T_H. As the degradation of exchange bias due to Mn interdiffusion only starts to develop for temperatures above 350 °C (ref. 21), there is a wide range of film temperatures (from 160 to 350 °C) under which patterning can be performed without causing sizeable irreversibility (Fig. 4 and related discussion). The fact that very demanding control of the tip temperature is not required is crucial for future applications.

To gain a deeper understanding of the micromagnetic configuration giving rise to the magnetic contrast observed with MFM, we performed micromagnetic simulations (see Supplementary Information) of the square, triangle and diamond patterns, as shown in Fig. 2f–h, respectively, where the black arrows indicate the orientation of the spins within the CoFeB film. The simulated out-of-plane component of the force on the ferromagnetic tip is presented in Fig. 2f–h using a blue–red (attractive–repulsive) colour code that can be associated with the dark–white contrast of MFM (see Supplementary Information for details). The agreement between simulations and experiments is very good for all patterns. It is worth noting that different kinds of 180° domain wall can be engineered by controlling the pattern shape. The fine details of the domain wall structure for each pattern are illustrated in the simulations in Fig. 2f–i, which show that by choosing the angle of the pattern side with respect to H_i and H_w, it is possible to tune the domain wall magnetic configuration.

The determination of the minimum feature size achievable by performing *tam*-SPL in our multilayer system was assessed by writing single lines with H_w antiparallel to H_i and with a spacing of 2 μm (Fig. 2d). The high-resolution MFM image in Fig. 2e of the dashed area in Fig. 2d shows that the average width of a single line, measured over a 2 μm section, is 300 nm, with a minimum of 250 nm. This demonstrates that, in this condition, the minimum spacing between lines during writing (allowing them to

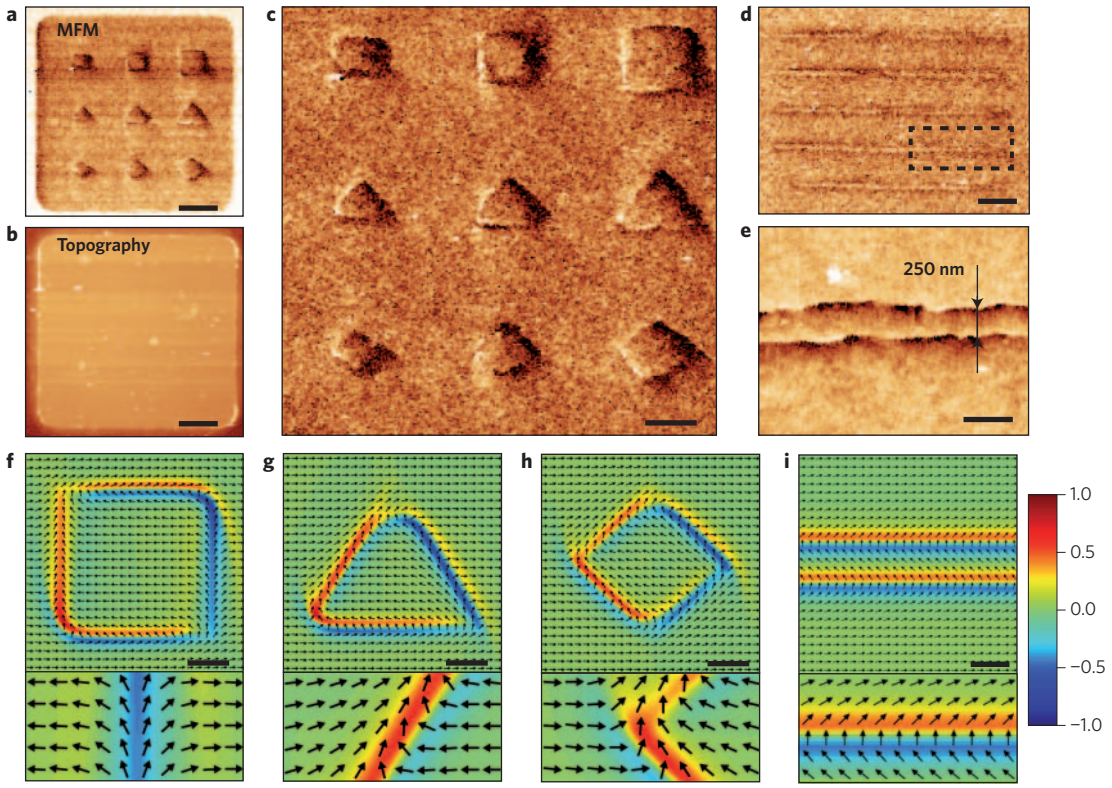

Figure 2 | MFM characterization and micromagnetic simulations of the patterned domain structures. a,**b**, MFM image (**a**) and topography (**b**) of the same pad after performing *tam*-SPL. The patterned domains are clearly visible in the MFM image, but no change is observed in the surface topography. **c**, Zoomed-in MFM image of square (top row), triangular (centre row) and diamond-shaped (bottom row) magnetic domains with dimensions of 2.5 μm (right column), 2 μm (centre column) and 1.5 μm (left column). The magnetic contrast marks the domain boundaries. **d**, MFM of single lines (12 μm long). **e**, High-resolution MFM image of the dashed rectangle in **d**, showing a minimum width of 250 nm. All MFM images were acquired under no external magnetic field. **f**–**i**, Micromagnetic simulation of the magnetic configuration of the patterned domains. Arrows indicate the direction of the spins, and the colour map shows the normalized magnetic force acting on the MFM tip. Bottom panels: zoomed-in view of the domain walls. In square structures (**f**), head-to-head and tail-to-tail domain walls are defined on the left and right sides, respectively, with the spins within the domain wall aligned along the wall. A different micromagnetic configuration is observed on the top and bottom sides, where the domain wall spins are perpendicular to the wall. In the triangle and diamond shapes (**g**,**h**), the arrangement of the spins within the wall is between the two cases described above. Scale bars: 4 μm (**a**,**b**), 2 μm (**c**,**d**), 500 nm (**e**), 1 μm (**f**–**h**), 250 nm (**i**).

keep their individuality) is on the order of 300 nm. The patterned lines present two domain walls of the same topology as those observed in the horizontal sides of the squares (Fig. 2f,i), with magnetization antiparallel with respect to the non-patterned area. The minimum feature size and the corrugation of the lines are determined both by the domain wall width, which depends on the micromagnetic properties of the system, and by the spatial profile of the exchange bias written by *tam*-SPL. Micromagnetic simulations indicate that the width of ideal 180° domain walls, with magnetization parallel to the wall far away from it, is on the order of 350 nm, in good agreement with the experimental width of the lines in Fig. 2e (Supplementary Fig. 8 and ref. 22). The spatial profile of the exchange bias is given by the finite width of the thermal profile produced by the hot tip in the antiferromagnet layer, as well as by the spatial distribution of the blocking temperatures of the system, which reflects the distribution of grain sizes in the antiferromagnet layer (see Supplementary Information). An improved spatial resolution and a reduced line corrugation can thus be achieved by optimizing the patterning conditions, the micromagnetic properties of the system[22] (for example, the exchange bias strength, magnetocrystalline anisotropy and exchange stiffness), the grain size distribution and the thermal properties of the materials[23].

Regarding the spatial confinement of the thermal profile, it has already been demonstrated that by performing *tc*-SPL on thermally insulating films[18], a 15 nm feature size can be achieved, which is at least comparable with state-of-the-art near-field transducers for magnetic recording technology[24]. For the writing speed, note that the crucial parameter is the time required to locally heat the sample above T_B. Further improvement, that is, down to 1 μs per point feature, could be obtained with a different thermal cantilever design[25].

In perspective, well-developed local heating technologies like those used in magneto-optical recording (MOR) and heat-assisted magnetic recording (HAMR) could be exploited for scaling up the presented approach[26–28].

Tunability and reconfigurability

Figure 3 shows that it is possible to finely tune the patterned magnetic anisotropy landscape by controlling the tip temperature. Figure 3a presents an MFM image taken in the remanent state for square areas patterned at $T_H = 100$, 240 and 435 °C (right to left in the figure) while applying $H_w = 700$ Oe antiparallel to H_i. When $T_H = 100$ °C, the local temperature of the sample is well below the blocking temperature, so no magnetic contrast is seen (blue square). Correspondingly, the shift in the local hysteresis loop measured with magneto-optical Kerr effect microscopy (μ-MOKE) along the UD anisotropy direction (Fig. 3b), approximately −50 Oe, is comparable to the shift of the loop (yellow loop in Fig. 3d) measured in the adjacent non-patterned area (yellow square in Fig. 3a). The patterned area written with $T_H = 240$ °C (green square) shows magnetic contrast, and the corresponding

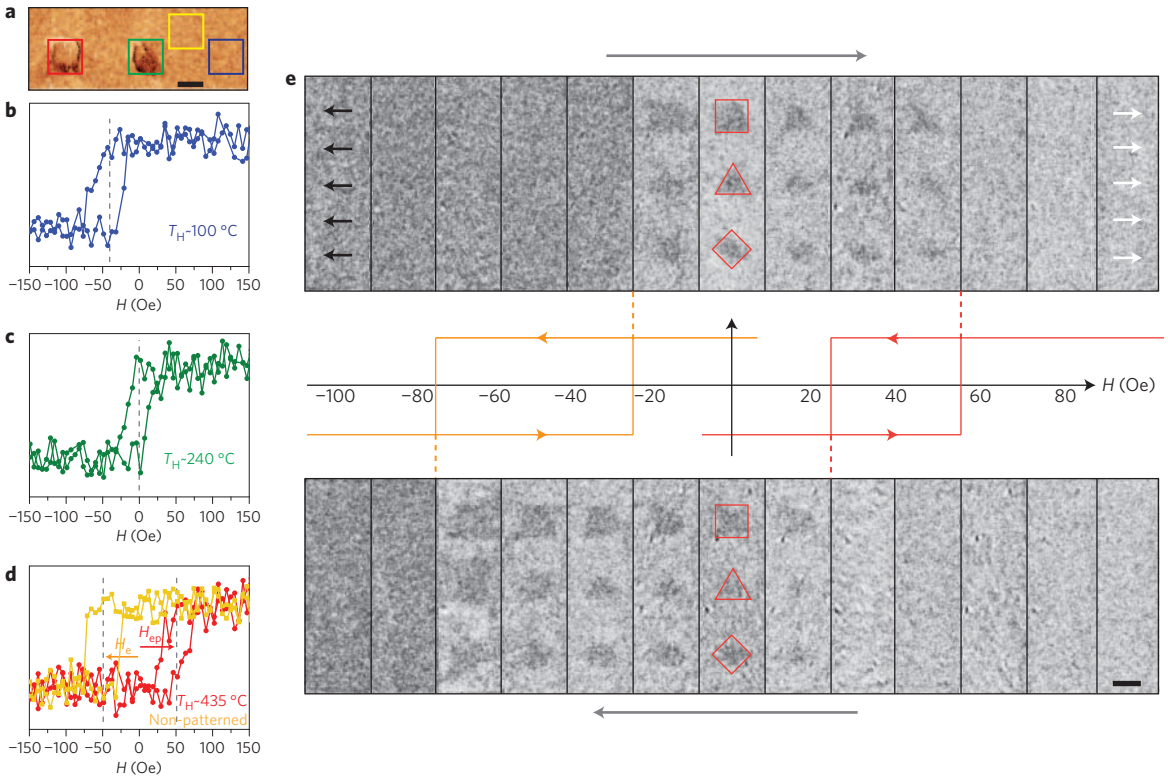

Figure 3 | Tunability of magnetic anisotropies and evolution of patterned domains with external magnetic field. a, MFM image at zero magnetic field from a non-patterned area (yellow square) and from areas patterned with T_H = 100 °C (blue square), 240 °C (green square) and 435 °C (red square), and H_w = 700 Oe. **b**–**d**, μ-MOKE hysteresis loops corresponding to the blue, green, and red and yellow squares in **a**, respectively. Starting from the initialized sample (yellow loop, H_e = –50 Oe), by increasing the heater temperature it is possible to tune the magnetic anisotropy and hence the exchange bias field (from H_{ep} = –50 Oe, blue loop; up to H_{ep} = +50 Oe, red loop). **e**, μ-MOKE frames from a movie acquired while sweeping a magnetic field parallel to the UD anisotropy axis, from –100 to +100 Oe (top sequence) and from +100 to –100 Oe (bottom sequence). At the beginning of the top sequence, the magnetization of both patterned and non-patterned areas lies in the negative direction (dark contrast); at around –20 Oe, the magnetization of the non-patterned film switches, giving rise to a bright contrast, while the patterned areas remain dark. The dark contrast eventually disappears at about +50 Oe, when the switching takes place also in the patterned areas. An analogue switching behaviour is observed in the bottom sequence. In the centre, the hysteresis loops from the non-patterned (yellow) and patterned (red) areas are sketched and the switching fields are marked. Scale bars, 2 μm (**a**,**e**).

local hysteresis loop (Fig. 3c) is centred at zero magnetic field. By increasing T_H to 435 °C (red square in Fig. 3a), the local hysteresis loop is eventually shifted to the right by +50 Oe (Fig. 3d), showing full inversion of the exchange bias field. The zero shift of the loop at 240 °C results from an incomplete exchange bias inversion due to the expected distribution of T_B in the film arising from the presence of grains with different size[15,29] (Supplementary Fig. 1). This demonstrates the possibility to pattern complex magnetic anisotropy landscapes in a continuous multilayer by tuning the heater temperature during writing. Moreover, by setting H_w at different angles with respect to H_i, areas can be patterned with the UD anisotropy axis arbitrarily oriented with respect to the film UD anisotropy set during initialization (Supplementary Fig. 3).

Analysis of the magnetic behaviour of the patterned area under an applied magnetic field, including the stability of the patterns, was carried out by μ-MOKE. Figure 3e presents some frames from a movie (Supplementary Movie 1), which show the field-induced evolution of the magnetization in the patterned area of Fig. 2c (right column). The appearance (disappearance) of the pattern is in agreement with the expected hysteresis loops of the patterned (non-patterned) regions, sketched in red (yellow). Furthermore—and crucial for technological applications—we have verified that the same remanent state (red shapes in Fig. 3e) is always recovered, even after 2,000 magnetization switching cycles performed with fields up to 1,000 Oe (data not shown), and that the patterns are stable six months after writing. Indeed, the

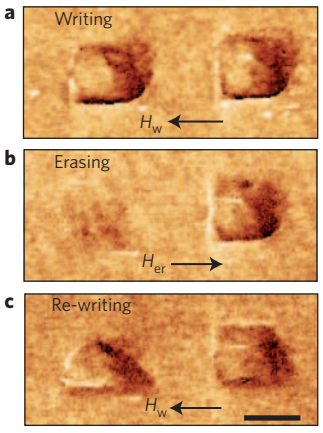

Figure 4 | Writing–erasing–rewriting capability. a, MFM image of two squares patterned with T_H = 600 °C and H_w = 700 Oe. **b**, The same area after erasure of the left square obtained by scanning it with T_H = 600 °C and an erasing field of H_{er} = –700 Oe, opposite to H_w and in the same direction as the initializing field H_i. **c**, A triangle is then rewritten on the left area with T_H = 470 °C and H_w = 700 Oe. Note that both the erasure and rewriting processes leave the right square unaffected. Scale bar, 2 μm.

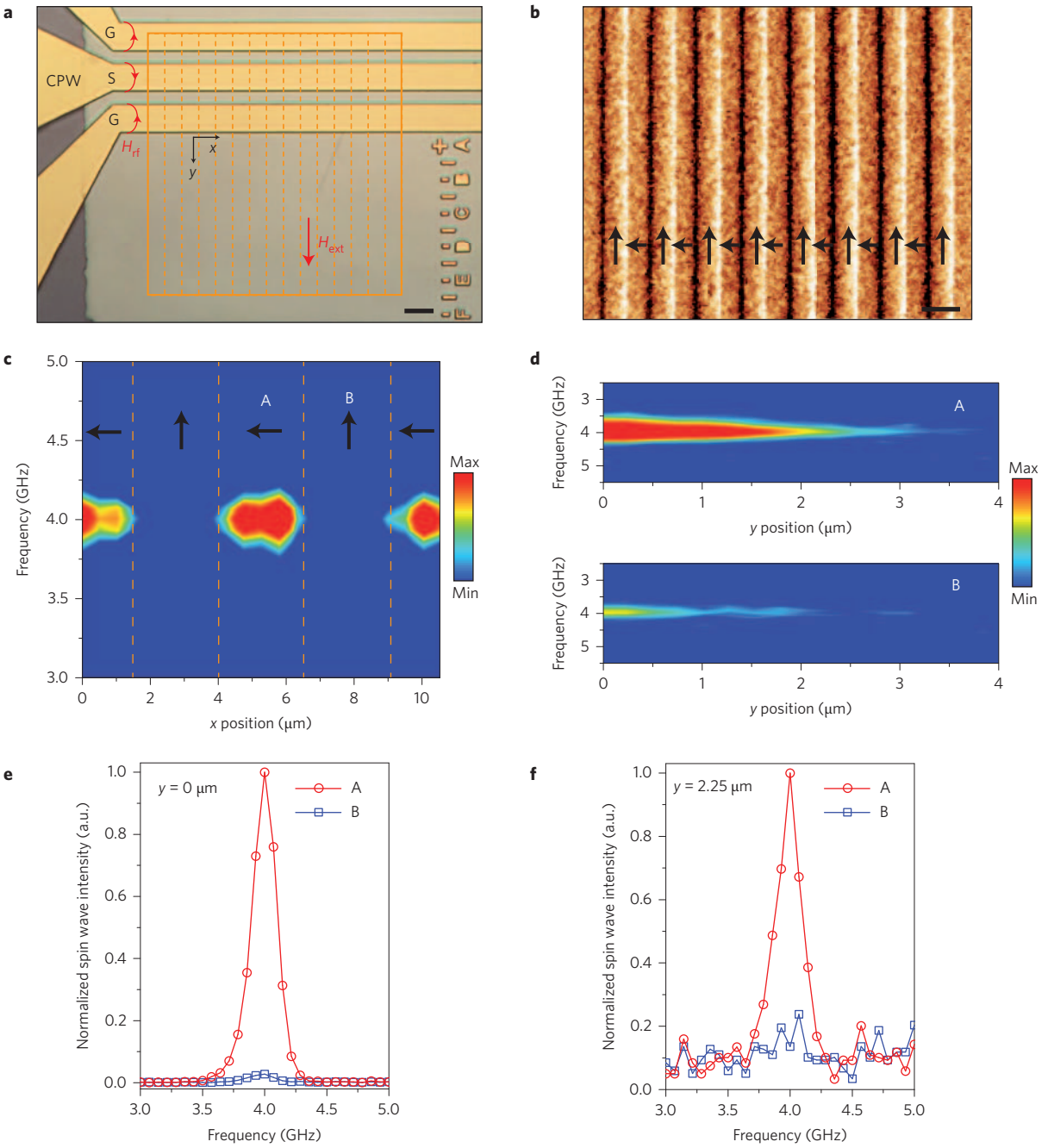

Figure 5 | Patterning magnonic structures. a, waveguide (CPW) generating the Oersted field H_{rf} and the pad where the *tam*-SPL patterning was performed. The orange rectangle marks the patterned area. Scale bar, 4 μm. **b**, MFM image of the magnonic structures, consisting of 2.5-μm-wide tracks with alternating 0° and 90° oriented remanent static magnetization (black arrows). The track boundaries are marked by dashed lines in **a**. Scale bar, 4 μm. **c**, One-dimensional map of the spin wave intensity measured at remanence by μ-BLS along the *x* direction (with a 0.5 μm step size), immediately outside the CPW. Spin waves are efficiently excited within tracks of type A. **d**, One-dimensional map of the spin wave intensity measured at remanence by μ-BLS as a function of distance *y* from the CPW (with a 0.25 μm step size). **e**,**f**, Spin wave spectra measured in track A (red circles) and track B (blue squares) at distances of $y = 0$ μm (**e**) and $y = 2.25$ μm (**f**) from the CPW.

resilience of the *tam*-SPL patterns is derived from the stability of the exchange bias, a key property that is also exploited in magnetic memory applications[30–33]. This feature can be used to implement a permanent functionality, similar to the case where magnetic devices are patterned by conventional techniques such as lithography and ion irradiation.

The reversibility of *tam*-SPL is illustrated in Fig. 4. Figure 4a shows a MFM image, under zero external field, of two squares patterned with $T_H = 600$ °C and $H_w = 700$ Oe antiparallel to H_i. Figure 4b shows the same area after local cancellation of the left square, achieved by scanning the same area with $T_H = 600$ °C in an erasing field of $H_{er} = -700$ Oe, opposite to H_w. The magnetic contrast almost completely disappears in the left square, but remains unperturbed in the right, indicating that the pattern has been selectively erased. Figure 4c shows that it is possible to rewrite the erased area with another shape, a triangle in this case, with $T_H = 600$ °C and $H_w = 700$ Oe. The pattern can also be completely erased by performing uniform field cooling, thus providing full

flexibility in writing and reversibly configuring the magnetic anisotropy landscape.

Magnonic applications

Here, we present a proof-of-concept experiment, performed by micro-focused Brillouin light scattering (μ-BLS), showing the potential applications of *tam*-SPL in the field of magnonics[34–38]. So far, magnonic devices have been fabricated by the physical patterning of magnetic thin films[39], modulating their thickness[40] or (as in the case of bi-component magnetic devices) creating a periodic array made of two magnetic materials[41]. Here, we propose to use *tam*-SPL to pattern magnonic structures in a continuous film, thus avoiding the scattering at physical interfaces created by standard lithography and providing an easy way to introduce reconfigurability and tunability into magnonics.

The investigated sample consisted of a 60 μm × 60 μm square pad, defined by optical lithography on the same multilayer structure in Fig. 2. *tam*-SPL was performed by applying H_w perpendicular to H_i to define 2.5-μm-wide tracks with alternating 0° and 90° oriented remanent magnetization over a total area of 38 μm × 39 μm (orange rectangle in Fig. 5a). The MFM image of the pattern at remanence is presented in Fig. 5b, where the black arrows indicate the magnetization direction within the pattern. The sharp transition between the two different magnetization configurations is marked by well-defined and sharp 90° domain walls.

Coplanar wave guides (CPWs), with a ground-to-ground distance of 12 μm and oriented perpendicular to the longitudinal direction of the *tam*-SPL tracks, were fabricated by electron-beam lithography and liftoff. μ-BLS measurements were then performed to map the spin wave intensity distribution.

Figure 5c shows the colour-coded spin wave intensity on a logarithmic scale measured at remanence, in the 3–5 GHz frequency range, as a function of the x position along the CPW arms. The BLS linear scan was performed just outside the CPW, at $y = 0$ in the reference system of Fig. 5a. The orange dashed lines mark the boundaries of the tracks, while the black arrows indicate the local direction of the static magnetization, which is parallel (perpendicular) with respect to the CPW in type A (B) tracks. Remarkably, propagating spin waves are efficiently excited only in type A tracks, whereas the spin waves' excitation efficiency is strongly reduced in type B tracks. A direct comparison of BLS spectra acquired just outside the CPW (Fig. 5e) shows that the spin wave intensity is about 36 times higher in the type A track (red circles) than in type B (blue squares).

Such behaviour can be explained by considering that, for this CPW geometry, spin waves are efficiently excited mainly by the coupling between the in-plane component of the microwave field (H_{rf} in Fig. 5a) and the corresponding component of the dynamical magnetization, associated with the spin waves, while the out-of-plane component of the microwave field plays a minor role. Within the pattern, the efficiency of the coupling is high in type A and low in type B tracks, depending on whether the in-plane component of the microwave field and the corresponding component of the dynamic magnetization are parallel or perpendicular[42,43].

Figure 5d shows the colour-coded spin wave intensity on a logarithmic scale acquired at remanence as a function of distance y from the CPW, in the centre of two adjacent tracks. We found that spin waves attenuate rapidly in the type B track (Fig. 5d, bottom), but in the type A track (Fig. 5d, top) they propagate efficiently over a distance comparable to that observed in Py and CoFe waveguides prepared by conventional lithographic techniques[44,45]. This result is confirmed by the BLS spectra acquired at $y = 2.25$ μm in tracks A and B (Fig. 5f). This finding can be explained taking into account that for perpendicular alignment of the spin waves wavevector and local magnetization, the group velocity of the spin waves is much larger than for parallel alignment[46].

The above result indicates that it is possible to locally control the spin wave excitation and propagation by creating remanent magnetization patterns via *tam*-SPL. This marks an initial step for the implementation of *tam*-SPL-based tunable and reconfigurable magnonic devices.

Supplementary Fig. 7 demonstrates the design of phase shifters and magnonic crystals exploiting the modulation of the refractive index seen by the spin waves in patterned regions with different relative orientation of the static magnetization and of the spin waves' wavevector. A single stripe can be used to implement a phase shifter to be inserted in Mach–Zehnder-type interferometers, which have been proposed as basic building blocks for computing[47]. In addition, a periodic arrangement of stripes such as those shown in Fig. 2d can be used to realize a magnonic crystal showing the emergence of characteristic bandgaps. The bandwidth and position of the bandgaps can be tuned by controlling the stripe width, their separation and the width of the regions of spin rotation between the stripes. Because all these parameters can be set reversibly during patterning, our technique allows the fabrication of fully reconfigurable magnonic crystals and devices. Moreover, active tuning of the magnonic properties after patterning can be achieved by controlling the domain extension and magnetization orientation via external magnetic fields (Fig. 3).

Conclusions

In this Article, we have introduced *tam*-SPL, a straightforward, single-step method for nanopatterning reprogrammable magnetic metamaterials, leaving the film chemistry and topography unperturbed. In particular, we have demonstrated the patterning of arbitrarily shaped magnetic micro- and nanostructures, with size down to 250 nm and remanent magnetization along an arbitrarily chosen direction, which are reconfigurable and stable against external magnetic perturbations. In perspective, further improvement of the spatial resolution could be achieved by optimizing the patterning parameters as well as the micromagnetic properties, thermal conductivity and granularity of the magnetic multilayer. A higher patterning speed could be obtained by using arrays of many heatable cantilevers[48] or using near-field transducers, allowing for highly localized and fast heating, with theoretical spot sizes down to 35 nm (ref. 24).

In addition, due to the extreme versatility of SPL, the magnetic patterning can be extended from continuous films to physically micro- and nanopatterned supports. Novel architectures for magnetic computing and spintronics can be envisaged, where reprogrammable magnetic metamaterials control the propagation of quasiparticles, such as domain walls in magnetic circuits, or spin waves and surface plasmons in magneto-plasmonic crystals. In particular, we have demonstrated local control of spin wave excitation and propagation in magnetic tracks patterned by *tam*-SPL. This result paves the way to the realization of reconfigurable and actively tunable devices, such as spin wave phase shifters and filters based on magnonic crystals.

Methods

Methods and any associated references are available in the online version of the paper.

Received 29 July 2014; accepted 4 February 2016; published online XX XX 2016

References

1. Schurig, D. *et al.* Metamaterial electromagnetic cloak at microwave frequencies. *Science* **314,** 977–980 (2006).
2. Zheludev, N. I. & Kivshar, Y. S. From metamaterials to metadevices. *Nature Mater.* **11,** 917–924 (2012).
3. Nikitov, S. a., Tailhades, P. & Tsai, C. S. Spin waves in periodic magnetic structures—magnonic crystals. *J. Magn. Magn. Mater.* **236,** 320–330 (2001).

4. Silva, A. *et al.* Performing mathematical operations with metamaterials. *Science* **343,** 160–164 (2014).
5. Temnov, V. V. Ultrafast acousto-magneto-plasmonics. *Nature Photon.* **6,** 728–736 (2012).
6. Maccaferri, N. *et al.* Resonant enhancement of magneto-optical activity induced by surface plasmon polariton modes coupling in 2D magnetoplasmonic crystals. *ACS Photon.* **2,** 1769–1779 (2015).
7. Kobljanskyj, Y. *et al.* Nano-structured magnetic metamaterial with enhanced nonlinear properties. *Sci. Rep.* **2,** 478 (2012).
8. Lenk, B., Ulrichs, H., Garbs, F. & Münzenberg, M. The building blocks of magnonics. *Phys. Rep.* **507,** 107–136 (2011).
9. Chumak, A. V., Vasyuchka, V. I., Serga, A. A. & Hillebrands, B. Magnon spintronics. *Nature Phys.* **11,** 453–461 (2015).
10. Monticelli, M. *et al.* On-chip magnetic platform for single-particle manipulation with integrated electrical feedback. *Small* http://dx.doi.org/10.1002/smll.201500916 (2015).
11. Chappert, C. Planar patterned magnetic media obtained by ion irradiation. *Science* **280,** 1919–1922 (1998).
12. Kim, S. *et al.* Nanoscale patterning of complex magnetic nanostructures by reduction with low-energy protons. *Nature Nanotech.* **7,** 567–571 (2012).
13. Ross, C. A. Patterned magnetic recording media. *Annu. Rev. Mater. Res.* **31,** 203–235 (2001).
14. Garcia, R., Knoll, A. W. & Riedo, E. Advanced scanning probe lithography. *Nature Nanotech.* **9,** 577–587 (2014).
15. Nogués, J. & Schuller, I. K. Exchange bias. *J. Magn. Magn. Mater.* **192,** 203–232 (1999).
16. Szoszkiewicz, R. *et al.* High-speed, sub-15 nm feature size thermochemical nanolithography. *Nano Lett.* **7,** 1064–1069 (2007).
17. Wang, D. *et al.* Thermochemical nanolithography of multifunctional nanotemplates for assembling nano-objects. *Adv. Funct. Mater.* **19,** 3696–3702 (2009).
18. Wei, Z. *et al.* Nanoscale tunable reduction of graphene oxide for graphene electronics. *Science* **328,** 1373–1376 (2010).
19. Kim, S. *et al.* Direct fabrication of arbitrary-shaped ferroelectric nanostructures on plastic, glass, and silicon substrates. *Adv. Mater.* **23,** 3786–3790 (2011).
20. Pires, D. *et al.* Nanoscale three-dimensional patterning of molecular resists by scanning probes. *Science* **328,** 732–735 (2010).
21. Fernandez-Outon, L. E., Araújo Filho, M. S., Araújo, R. E., Ardisson, J. D. & Macedo, W. A. A. Setting temperature effect in polycrystalline exchange-biased IrMn/CoFe bilayers. *J. Appl. Phys.* **113,** 17D704 (2013).
22. Albisetti, E. & Petti, D. Domain wall engineering through exchange bias. *J. Magn. Magn. Mater.* **400,** 230–235 (2016).
23. Algré, E., Gaudin, G., Bsiesy, A. & Nozières, J. Improved patterned media for probe-based HAMR. *IEEE Trans. Magn.* **41,** 2857–2859 (2005).
24. Miao, L., Stoddart, P. R. & Hsiang, T. Y. Novel aluminum near field transducer and highly integrated micro-nano-optics design for heat-assisted ultra-high-density magnetic recording. *Nanotechnology* **25,** 295202 (2014).
25. King, W. P., Bhatia, B., Felts, J. R., Kim, H. J. & Kwon, B. Heated atomic force microscope cantilevers and their applications. *Annu. Rev. Heat Transf.* **XVI,** 287–326 (2013).
26. Wu, A. Q. *et al.* HAMR areal density demonstration of 1 + Tbpsi on spinstand. *IEEE Trans. Magn.* **49,** 779–782 (2013).
27. Saito, J., Sato, M., Matsumoto, H. & Akasaka, H. Direct overwrite by light power modulation on magneto-optical multi-layered media. *Jpn J. Appl. Phys.* **26,** 155–159 (1987).
28. Stanciu, C. *et al.* All-optical magnetic recording with circularly polarized light. *Phys. Rev. Lett.* **99,** 047601 (2007).
29. O'Grady, K., Fernandez-Outon, L. E. & Vallejo-Fernandez, G. A new paradigm for exchange bias in polycrystalline thin films. *J. Magn. Magn. Mater.* **322,** 883–899 (2010).
30. Petti, D. *et al.* Storing magnetic information in IrMn/MgO/Ta tunnel junctions via field-cooling. *Appl. Phys. Lett.* **102,** 192404 (2013).
31. Marti, X. *et al.* Room-temperature antiferromagnetic memory resistor. *Nature Mater.* **13,** 367–374 (2014).
32. Prejbeanu, I. L. *et al.* Thermally assisted MRAMs: ultimate scalability and logic functionalities. *J. Phys. D* **46,** 074002 (2013).
33. Papusoi, C. *et al.* Reversing exchange bias in thermally assisted magnetic random access memory cell by electric current heating pulses. *J. Appl. Phys.* **104,** 013915 (2008).
34. Camley, R. E. *et al.* High-frequency signal processing using magnetic layered structures. *J. Magn. Magn. Mater.* **321,** 2048–2054 (2009).
35. Kim, S.-K., Lee, K.-S. & Han, D.-S. A gigahertz-range spin-wave filter composed of width-modulated nanostrip magnonic-crystal waveguides. *Appl. Phys. Lett.* **95,** 082507 (2009).
36. Chumak, A. V., Serga, A. A. & Hillebrands, B. Magnon transistor for all-magnon data processing. *Nature Commun.* **5,** 4700 (2014).
37. Krawczyk, M. & Grundler, D. Review and prospects of magnonic crystals and devices with reprogrammable band structure. *J. Phys. Condens. Matter* **26,** 123202 (2014).
38. Csaba, G., Papp, A. & Porod, W. Spin-wave based realization of optical computing primitives. *J. Appl. Phys.* **115,** 17C741 (2014).
39. Neusser, S. & Grundler, D. Magnonics: spin waves on the nanoscale. *Adv. Mater.* **21,** 2927–2932 (2009).
40. Gubbiotti, G. *et al.* Collective spin waves on a nanowire array with step-modulated thickness. *J. Phys. D* **47,** 105003 (2014).
41. Tacchi, S. *et al.* Forbidden band gaps in the spin-wave spectrum of a two-dimensional bicomponent magnonic crystal. *Phys. Rev. Lett.* **109,** 137202 (2012).
42. Kalinikos, B. A. Excitation of propagating spin waves in ferromagnetic films. *IEE Proc. H* **127,** 4 (1980).
43. Brächer, T. *et al.* Generation of propagating backward volume spin waves by phase-sensitive mode conversion in two-dimensional microstructures. *Appl. Phys. Lett.* **102,** 2011–2016 (2013).
44. Vogt, K. *et al.* Realization of a spin-wave multiplexer. *Nature Commun.* **5,** 3727 (2014).
45. Urazhdin, S. *et al.* Nanomagnonic devices based on the spin-transfer torque. *Nature Nanotech.* **9,** 509–513 (2014).
46. Stancil, D. D. & Prabhakar, A. *Spin Waves Theory and Applications* (Springer, 2009).
47. Schneider, T. *et al.* Realization of spin-wave logic gates. *Appl. Phys. Lett.* **92,** 022505 (2008).
48. Carroll, K. M. *et al.* Parallelization of thermochemical nanolithography. *Nanoscale* **6,** 1299–1304 (2014).

Acknowledgements

E.A. thanks K. Carroll, L. Xi and P. Sarti for discussions. M.M. and S.T. thank G. Carlotti for discussions. E.A. and E.R. acknowledge the support of the Office of Basic Energy Sciences of the US Department of Energy (DE-FG02-06ER46293). E.R. acknowledges partial support from the National Science Foundation (NSF; grant no. CMMI 1436375). E.A. and D.P. acknowledge support from Cariplo project UMANA (project no. 2013-0735). R.B. acknowledges support from Cariplo project MAGISTER (project no. 2013-0726). M.M. and S.T acknowledge support from the Ministero Italiano dell'Università e della Ricerca (MIUR) under the PRIN2010 project (no. 2010ECA8P3). M.P. and P.V. acknowledge support from the Basque Government (program no. PI_2015_1_19) and (M.P.) from the Spanish Ministry of Economy Competitiveness (grant no. BES-2013-063690). This work was partially performed at Polifab, the micro- and nanofabrication facility of the Politecnico di Milano.

Author contributions

E.A., with the help of D.P., conceived and designed the experiments. E.R. and R.B. coordinated and supervised the research. E.A. performed patterning experiments, MFM characterization and simulations. D.P. fabricated the samples. W.P.K. provided the thermal SPM tips. E.A., M.P., P.V. and R.B. performed MOKE characterization. E.A. and D.P. fabricated the samples for μ-BLS measurements. M.M. and S.T. performed μ-BLS measurements. A.P., G.C. and W.P. performed the simulation of the magnonic structures. E.A., D.P., M.M., S.T., P.V., E.R. and R.B. wrote the manuscript. All authors contributed to discussions regarding the research.

Additional information

Supplementary information is available in the online version of the paper. Reprints and permissions information is available online at www.nature.com/reprints. Correspondence and requests for materials should be addressed to E.A., E.R. and R.B.

Competing financial interests

The authors declare no competing financial interests.

Methods

Sample fabrication and characterization. $Co_{40}Fe_{40}B_{20}$(5 nm)/$Ir_{22}Mn_{78}$(7 nm)/Ru (2 nm) stacks were deposited on Si/SiO_2(1,000 nm) substrates by d.c. magnetron sputtering using an AJA Orion8 system with a base pressure below 1×10^{-8} torr. During deposition, a 300 Oe magnetic field (H_G) was applied in the sample plane to set the magnetocrystalline uniaxial (UA) anisotropy direction in the CoFeB layer and the exchange bias direction in the as-grown sample. Both the critical temperature at which the exchange bias disappears (blocking temperature T_B) and the exchange bias strength decrease with antiferromagnetic layer (IrMn) thickness. We used a 7 nm IrMn layer, as this thickness ensures both a strong exchange bias and a T_B above room temperature (160 °C, as shown in Supplementary Fig. 1), allowing local field cooling to be performed by scanning the heatable SPM tip. For the ferromagnet, the 5 nm CoFeB thickness ensures both a sizeable exchange bias, which decreases for higher ferromagnet thickness[15], and a straightforward characterization of the magnetic domains by MFM and μ-MOKE. The multilayer surface roughness measured in a 1 μm^2 area is 0.15 nm (root mean square). Squared pads with a 400 μm^2 area were microfabricated by optical lithography and ion milling, allowing for the individuation of the magnetic patterns defined by *tam*-SPL. After microfabrication, to set the UD anisotropy axis in the CoFeB film, the samples underwent field cooling starting at 220 °C (above blocking temperature T_B) in vacuum and in a 4,000 Oe magnetic field H_i applied along the UA axis of the CoFeB film. The magnetic characterization of the stacks was performed in a Microsense vibrating sample magnetometer equipped with a heater for temperature-dependent measurements.

***tam*-SPL.** *tam*-SPL was performed with a modified Agilent 5500 SPM system equipped with custom-made silicon SPM cantilevers integrated with a Joule-heating resistive heater[17,18,25]. Details about these thermal cantilevers and temperature calibration are provided in the Supplementary Information. A National Instruments NI cDAQ-9178 was used to control and record the current passing through the cantilever to achieve Joule heating. To pattern arbitrary one- or two-dimensional geometries, such as lines, polygons and complex planar shapes, MATLAB scripts were used in combination with Agilent PicoView software. The magnetic patterns were written by raster-scanning the heated tip in contact mode using a linear speed of 3 μm s^{-1}. Two permanent magnets were used to generate the uniform 700 Oe external magnetic field applied in the sample plane during patterning. An arbitrary angle between the direction of the external field and the initialization direction of the sample was set by physically rotating the sample with respect to the magnets.

MFM characterization. MFM characterization of the patterned magnetic domains was performed with the same Agilent 5500 SPM system used for *tam*-SPL, but equipped with a Nanosensors PPP-MFMR AFM magnetic probe. MFM imaging was performed in lift mode, with lift heights of 100 nm (Figs 2a,c,d, 3a, 4 and 5b and Supplementary Figs 3 and 4) and 30 nm (Fig. 2e).

μ-MOKE characterization. To conduct investigations of the magnetization distribution at the sub-micrometre length scale we used a characterization tool based on magneto-optic Kerr effect imaging/magnetometry based on an optical wide-field polarization microscope optimized for Kerr microscopy (Evico). Arbitrary magnetic fields can be applied during observation so that domain nucleation and magnetization processes can be observed. Indeed, the domain contrast in the image is directly sensitive to the projection of the magnetization along the sensitivity direction, which is set either parallel or perpendicular to the externally applied field. For this purpose, the microscope was equipped with a rotatable bipolar electromagnet that allowed the application of a magnetic field with intensity up to 5,000 Oe along an arbitrary direction in the sample plane. Two different operational modes of the microscope were used: (1) with a high-sensitivity and high-resolution charge-coupled device (CCD) camera, magnetic contrast imaging of the sample surface was performed with a spatial resolution of ~500 nm; (2) the CCD camera was used as a conventional photodetector to measure the local magnetization reversal (hysteresis loops) by selecting an arbitrary region of interest (ROI) and thus a limited number of pixels. At maximum optical magnification (×100 objective followed by a ×4 tube lens), each CCD pixel corresponded to an area of 15×15 nm^2 of the sample surface. Single-shot hysteresis loops of sample surface portions as small as 1×1 μm^2 were measured[49].

BLS microscopy measurements. μ-BLS measurements were performed by focusing about 5 mW of monochromatic light (from a diode-pumped solid-state (DPSS) laser operating at a spectral line of 532 nm) with a microscope dark-field objective of large numerical aperture (NA = 0.75) and super-long working distance (4.7 mm)[50]. Using the same objective, a coaxial viewing system based on a collimated light-emitting diode (LED) light source (455 nm wavelength), a beam expander and a CCD camera was implemented into the set-up to obtain a direct visualization of the laser spot and of the sample region under investigation. Electrical access to the sample was achieved using a specially designed ground–signal–ground (GSG) antenna with large extended pads where a d.c. was injected with a picoprobe.

During μ-BLS measurements the sample holder and BLS spectrometer were controlled by TFPDAS4-MICRO and TFPDAS4 software, developed at Kaiserslautern University, which provided active stabilization of the lateral and vertical positions of the sample with a precision of ~50 nm.

References

49. Nikulina, E., Idigoras, O., Vavassori, P., Chuvilin, A. & Berger, A. Magneto-optical magnetometry of individual 30 nm cobalt nanowires grown by electron beam induced deposition. *Appl. Phys. Lett.* **100,** 142401 (2012).
50. Madami, M., Gubbiotti, G., Tacchi, S. & Carlotti, G. in *Solid State Physics* Vol. 63 (eds Camley, R. E. & Stamps, R. L.) 79–150 (Academic, 2012).

Journal: Nature Nanotechnology

Article ID: nnano.2015.25

Article title: Nanopatterning reconfigurable magnetic landscapes via thermally assisted scanning probe lithography

Author(S): Albisetti *et al.*

Query no.	Queries	Response
Q1	Please check that the affiliations are correct as expanded	
Q2	Please check that the abstract is OK as amended	
Q3	Can we be more specific about where you mean in the Supplementary Information? A section number or heading perhaps?	
Q4	By “in this condition” do you mean “under these conditions”? Please check.	
Q5	By “allowing them to keep their individuality”, do you mean “allowing them to keep their individual definition” or similar?	
Q6	I am not sure what you mean by “In perspective” – do you mean “In the future”?	
Q7	Please check that the sentence beginning “Correspondingly” is OK as amended	
Q8	Please check that the sentence beginning “The patterned area” is OK as amended	
Q9	Please check that the sentence beginning “*tam*-SPL was performed” is OK as amended	
Q10	Do you mean the orange dashed lines in Figure 5c?	
Q11	Do you mean “are parallel or perpendicular to one another”?	
Q12	Please provide updated information for ref 10 (volume number and page range/article number)	
Q13	Ref 26 – please check inserted journal name	
Q14	Ref 41 – please check inserted article number	
Q15	Ref 42 – please insert end page (unless this is provided as an article number)	
Q16	Please check that the acknowledgements are OK as	

	amended	
Q17	Figure 4c – the value of T_H does not appear to be the same as that given in the main text – please text	
Q18	I am not sure what you mean by “individuation” here – do you mean “distinct”?	
Q19	Here, do you mean “with large extended pads into which a d.c. current was injected with a picoprobe”?	